Drag coefficient prediction for non-spherical particles in dense gas–solid two-phase flow using artificial neural network

Shengnan Yan, Yurong He *, Tianqi Tang, Tianyu Wang

School of Energy Science and Engineering, Harbin Institute of Technology, Harbin 150001, China

ARTICLE INFO

ABSTRACT

Artificial neural network (ANN) was adopted to predict and analyze the relationship of drag coefficient, Reynolds number, and sphericity for non-spherical particles in dense gas–solid two-phase flow. We first employed Back Propagation Neural Network (BPNN) and Radial Basis Function Neural Network (RBFNN) to predict drag coefficients based on experimental results (Pettyjohn, 1948; Yow et al., 2005). Comparisons between simulation and experimental results indicate that RBFNN efficiently predicts the drag coefficients with as high precision as BPNN. Furthermore, we made predictions and analyses of drag coefficients under different sphericities employing Radial basis function neural network. Results reveal that artificial neural network is applicable in predicting and investigating drag coefficient in gas–solid non-spherical particulate systems. Based on the predicted results of drag coefficients, we conducted a curve fitting of drag coefficient, Reynolds number, and particle sphericity, obtaining a correlation on drag coefficient. Incorporating the drag coefficient correlation with Syamlal-O'Brien and Gidaspow-blend model, simulation on gas–solid two-phase flow by Eulerian–Eulerian model was carried out from fixed beds to bubbling fluidized beds. Simulation pressure drop are compared with experimental results obtaining a good agreement with each other, which indicates that the drag force of non-spherical particles in a gas–solid system could be predicted reasonably by an artificial neural network method. This work provides a reference for predicting drag coefficients of particles with complex shape in gas–solid two-phase system.

© 2019 Elsevier B.V. All rights reserved.

1. Introduction

The transport of particles in gas–solid two-phase flow is very common in a wide range of research fields and applications, from industrial (coating, drying, granulation, synthesis of base chemicals, gasification, and combustion) [3–5] to natural processes (sedimentation of solid particles in rivers and during explosive eruptions) [6,7]. Figuring out particles' behavior in dense gas–solid flow is very crucial for the successful and effective design, operation, optimization and scale-up of fluidized bed reactor in many important industrial applications, such as drying of solids, numerous synthesis reactors and pulverized coal combustors [8–10]. In practical applications, the particles employed generally are non-spherical [11], including regular (e.g. cylinder, cube, disk, ellipsoid, tetrahedron) and irregular shapes (e.g. pulverized biomass, splinters, flakes, sand, agglomerates) [12]. Nonetheless, dealing with particulate flows, researchers frequently assume particles to be perfectly spherical. This oversimplified assumption is mainly due to the fact that characterizing non-spherical particles is complex and model simplicity brings a fast computation. However, previous studies reveal that particle shape has a strong influence on gas–solid drag force [13], which plays a

dominant role in gas–solid fluidization. Particles' shape affects the statics and dynamics of granular systems [14–16] not only by changing the values of the experienced forces and torques but also by shifting the Reynolds number at which the transition to unsteady flow occurs [17]. It is one of the dominant mechanisms for interphase momentum transfer. Thus, neglecting the effect of particle shape will not provide convincing and satisfactory results.

Drag coefficient plays a dominant role in determining drag force. A great many experiments have been conducted to measure drag coefficients, including particle settling experiments at a low *Re* and wind tunnel experiments at a high *Re* [18]. Based on the experimental data, researchers proposed miscellaneous formulas to predict drag coefficient of spherical and non-spherical particles. Haider and Levenspiel [19] correlated the reported experimental data and proposed the following general form of drag correlation for spherical and non-spherical particles. It is available in the Reynolds number range $<2.6 \times 10^5$. Swamee and Ojha [20] introduced Corey shape factor and proposed a drag correlation based on this parameter. Ganser [21] proposed that every particle experiences a Stokes' regime where drag is linear in velocity and a Newton's regime where drag is proportional to the square of velocity [22]. Stokes shape factor and Newton shape factor are introduced. Then they put forward a drag expression. Chien et al. [23] reported a simple expression of drag based on data from petroleum engineering and processing

* Corresponding author.
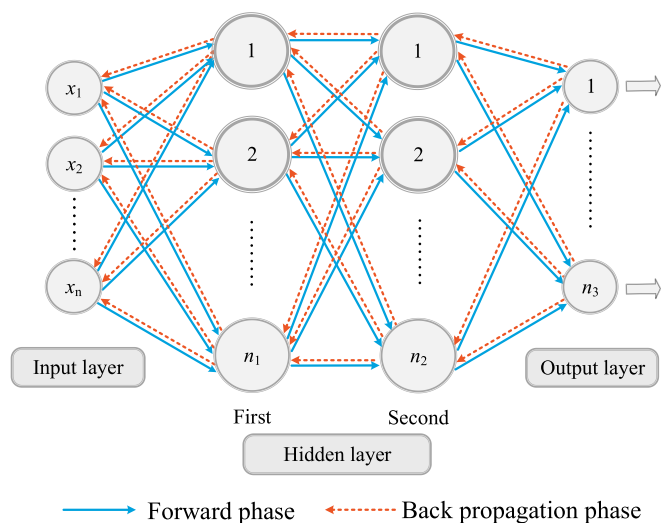 *E-mail address:* rong@hit.edu.cn (Y. He).

Fig. 1. An illustration of BPNN architecture [32].

literature. Hartman et al. [24] proposed a drag correlation for predicting steady-state, free-fall conditions of non-spherical, isometric particles. Tran-Cong et al. [25] experimentally studied the steady-state free-fall conditions of isolated groups of ordered packed spheres through Newton fluids. Drag coefficients particles with six different shapes, isometric, axisymmetric, orthotropic, plane and elongated conglomerates of spheres, were measured. Yow et al. [2] derived a drag correlation from the Kaskas equation. Hölzer et al. [18] accounted for the particle orientation over the entire Reynolds number range. Besides sphericity, crosswise sphericity and lengthwise sphericity were used in the drag correlation. Dioguardi and Mele [6] applied particle shape factor, which is the ratio of sphericity and circularity. They measured drag coefficients of non-spherical particles sampled from volcanic material. The experiments cover a Reynolds number of 0.1 to 10,000. Song et al. [26] studied settling behaviors of spheres, cubes, and cylinders in Newtonian fluids. A parameter, which is the ratio between equivalent sphere area and the projected area of particle settling direction, was utilized to characterize the shape of particles. Their proposed drag correlation is valid with particle Reynolds number ranging from 0.001 to 100 and sphericity ranging from 0.471 to 1. It is especially suitable for spherical, cubic, and cylindrical particles.

Recently settling experiments are tested in a cylindrical column with a height of 1500 mm and an inner diameter of 100–200 mm. Different solutions of glycerine and distilled water are employed as test fluid. Generally, researchers load test fluid into the fall column at least one day before each experimental session. This approach can extrude the air bubble, which can modify the physical property of solution. To ensure a perfect particle liquid contact, particles should keep soaked in the solution for two days before running the experiment. Then each particle is dropped in the center of the column at least three times and its movement is captured by a high-speed camera [26]. Particle settling experiment is a time-consuming process and easy to be influenced by temperature and pressure of testing environment. For a high *Re* (*Re* > 1000), researchers applied a wind tunnel to measure drag coefficients. The upward airflow makes the particles suspend in the test section. Similarly, a high-speed camera records the movement of particles. More details of constructing a wind tunnel and measuring drag coefficients can be found in Bagheri et al.'s work [27,28]. A wind tunnel is hard and complicated to design. Building a wind tunnel costs a lot of time and money and occupies much laboratory space. Both of the two methods have a high demand for manpower and material resources. Note that if drag coefficients of non-spherical particles that have not been tested before are needed, the same process should be repeated again.

In order to avert doing extensive experiments to obtain drag coefficients, we adopted an artificial neural network (ANN) method to predict drag coefficients. ANN, inspired by biological neural networks constituting human brains, is a computational method that consists of processing elements (called neurons), and connections between them with coefficients (weights) bound to the connections [29]. In 1943, McCulloch and Pitts first proposed the conception of the artificial neuron [30]. In 1949, based on hypothesis and observations of neurophysiologic, Hebb first put forward a approach to train ANN (Hebb's rule) [31]. Over the following fifty years, the research on ANN was stuck in the doldrums. On early 1990s, this subject regained attention and has been deeply researched until now. ANN still abounds in research potential. ANN has several remarkable advantages, such as adapting from experience, learning capability, generalization capability, data organization, fault tolerance, distributed storage, facilitated prototyping and so on. Due to these key features, ANN is potential to apply in multiple areas of science and engineering, including universal curve fitting, process control, pattern recognition, data clustering, system prediction and optimization, associative memory, etc. [32]. ANN is primarily linked with prediction, regression, classification, and principal component analysis. With respect to energy, researchers focus more on the combination of ANN with renewable energy, heat transfer, and particle swarm optimization. In the field of biology, ANN is mainly applied to study fermentation, cancer, biomass, and diagnosis. Personnel from chemical engineering put more effort in studying adsorption, response-surface methodology, central composite design combined with ANN. In terms of material science, ANN is frequently connected with the research of mechanical property, microstructure, and performance. For medicine, ANN plays a crucial role in diagnosing breast cancer, principal component analysis, and texture analysis. Associated with ANN, computer science primarily deals with wavelet transform, genetic algorithms, fault diagnosis and image processing.

Recently, some researchers are employing ANN modeling in the study of fluidization. Maiti et al. [33] successfully applied ANN model to predict the minimum fluidization velocity. Farizhandi et al. [34] used ANN model to model change in particle size distribution in a gas–solid fluidized bed. To our knowledge, little work has been reported on predicting drag coefficients of non-spherical particles using ANN model. In this paper, we compared the performance of two different ANN models in predicting drag coefficients for a dense gas–solid particulate system. Our aim is to test the feasibility and efficiency of ANN for investigating drag coefficients and developing a new way to obtain drag coefficient for non-spherical particle systems.
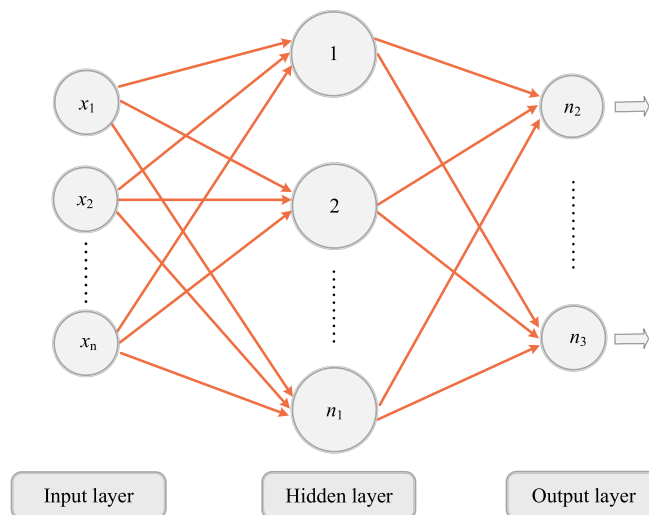

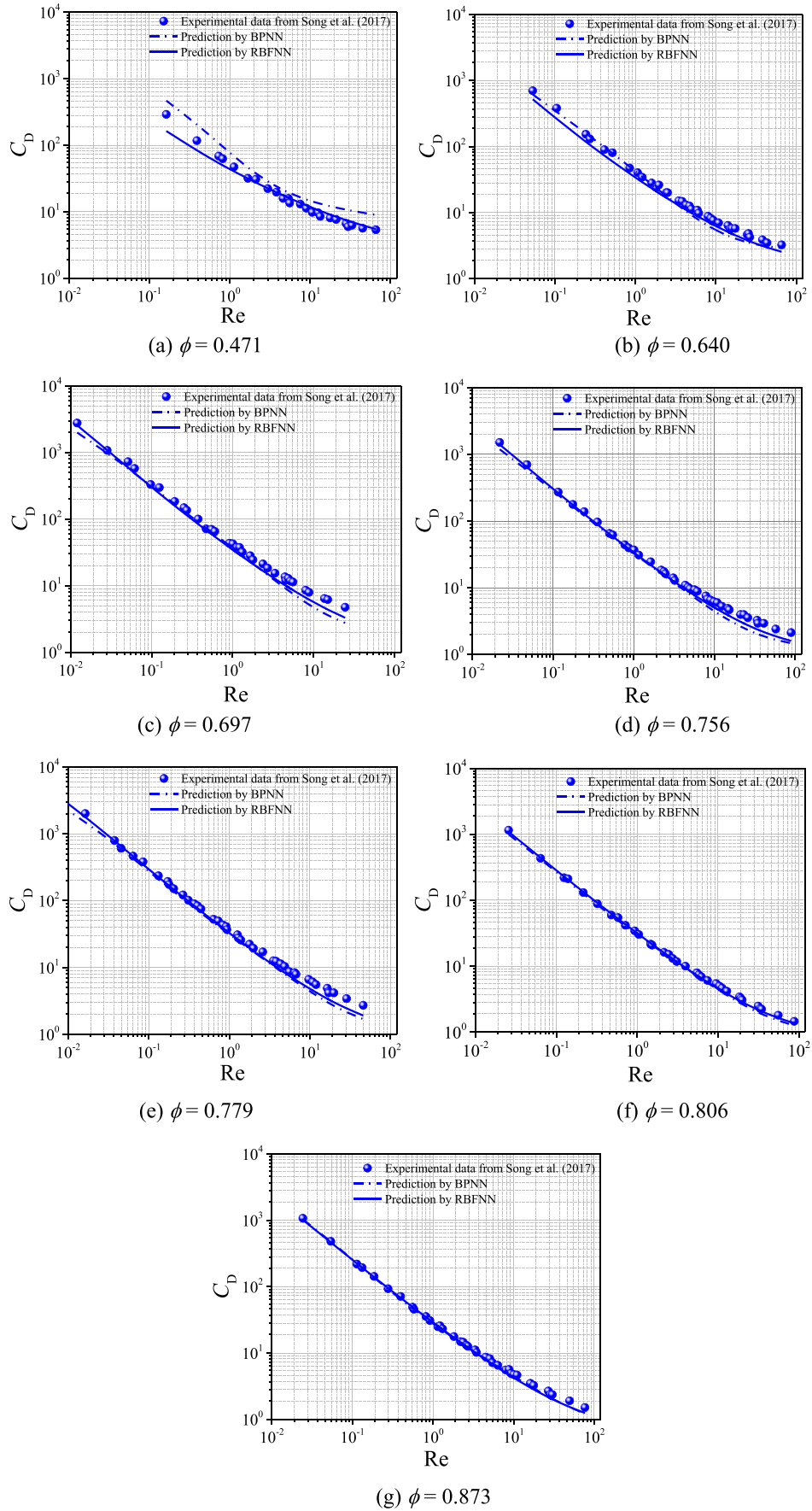**Fig. 2.** Basic Structure of RBFNN [39].

Fig. 3. Comparison between prediction results by BPNN and RBFNN and experimental results of Song et al. [26].
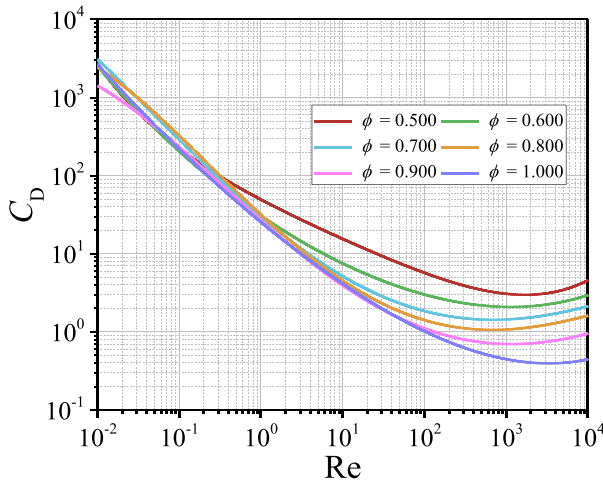
Fig. 4. Drag coefficient prediction by RBFNN.

2. Artificial neural network model

Generally speaking, an artificial neural network is composed of three layers: input layer, hidden (intermediate) layer, and output layer [32]. Information within the network starts from the input layer, passes through the hidden layers, and ends in the output layer. From the external environment, input layer obtains information, signals, features, or measurements. Activation functions generate limit values, then make a normalization of the inputs. The neurons inside the hidden layer extract patterns for the process or system to be analyzed. Output layer produces and shows the final network outputs that originate from the processing conducted by the neurons in the preceding layers. ANN has an ability to learn and improve its performance from examples, which is its fundamental trait [35]. In this work, two typical ANN models, back propagation neural network model and radial basis function neural network model, were adopted and introduced.

2.1. Back propagation neural network model (BPNN)

In 1986, Rumelhart, Hinton and Williams proposed the back propagation (BP) algorithm for setting weights and hence for the training of multi-layer perceptrons (MLP) [36,37]. In the learning process, a supervised learning algorithm is executed in the form of the neural network associate memory. BPNN learning mechanism is composed of forward propagation and back propagation phase. Initially, a random weight vector is adopted. In the forward phase, learning sample is fed into the input layer. Based on the initial weight vector, an output vector is obtained. Then an error between output vector and target output vector is calculated. In the back propagation phase, the optimal solution is located via a gradient descent in the weight space. Layer by layer, the abovementioned error is propagated back from output units to input units. Weight vectors are adjusted to minimize the error in the process of propagation. The learning process is finished until a convergence of error function is achieved. An architecture of typical BPNN is presented in Fig. 1.

2.2. Radial basis function neural network (RBFNN)

Radial basis function neural network (RBFNN) was addressed by Broomhead et al. in 1988 [38]. Based on local response characteristics of biological neurons, they introduced radial basis function into the design of neural network. RBFNN consists of three layers: one input layer, one hidden layer, and only one output layer. RBFNN has a good generalization ability and a simple network structure that avoids unnecessary and lengthy calculation as compared to the multilayer feed-forward network (MFN) [39]. The hidden layer is made up of an array of computing units called hidden nodes. In the hidden layer, the activation function is Gaussian. The working principle of RBFNN is somewhat similar to BPNN. Signals of the learning sample is propagated from the hidden layer to the output layer. Notably, RBF learning process has two unique stages. In the first stages, a self-organized learning method, which is merely dependent on the trait of the input data, is adopted to make an adjustment of the weights of the neurons. This adjustment allocated the radial basis functions. In the second stage, the generalized delta rule adjusts the weight of the neurons in the output layer. Furthermore, RBFNN learning process begins from the hidden layer and stops at the output layer. A typical configuration of an RBFNN is displayed in Fig. 2.

In this paper, Reynolds number and sphericity are input parameters, while drag coefficient is the output parameter. We collected data from literatures and used them for training and learning. Then we made predictions of drag coefficients and analyzed the variation that drag coefficients changed with Reynolds number under different sphericities. The neurons belonging to the hidden layer of the RBFNN consists of activation functions with radial basis. The Gaussian activation function is one of the most used [32].

$$g(u) = e^{-\frac{(u-c)^2}{2\sigma^2}} \tag{1}$$

where c is the center of the Gaussian function and σ^2 denotes its variance. The higher the variance value, the larger is the base of the function. The following part presents the first training stage of RBFNN. Obtain the
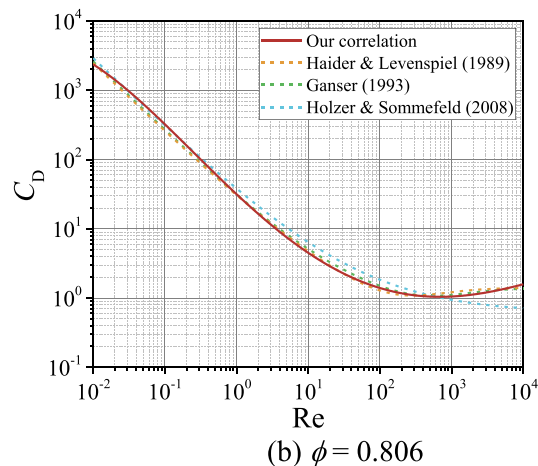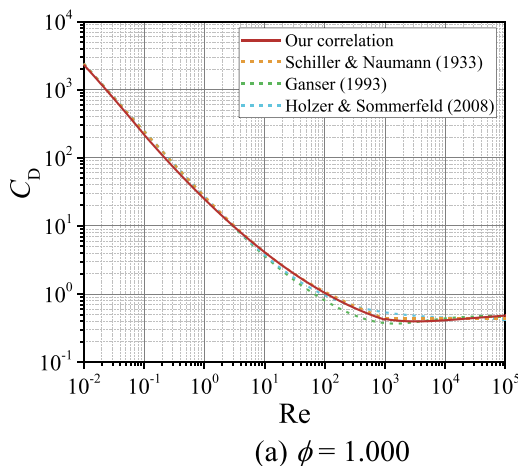

(a) $\phi = 1.000$

(b) $\phi = 0.806$

Fig. 5. Drag coefficients comparison for spherical particle and non-spherical particle.
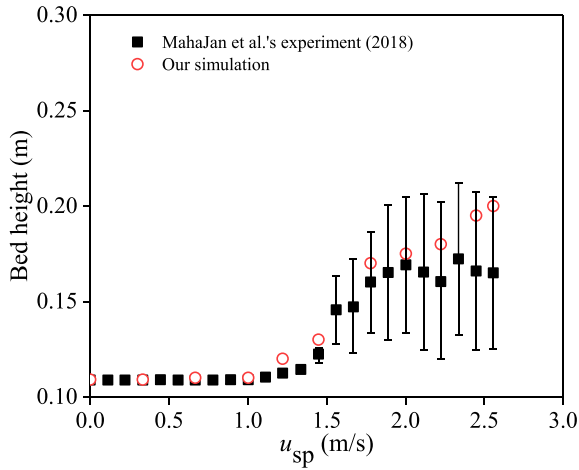
Fig. 6. Bed height distribution under different superficial gas velocities.

set of training samples firstly. Initialize the weight vector of each neuron of the hidden layer with the values of the first training samples. Then the following steps are repeated until there are no more changes in the groups between two iterations. For all the samples of Reynolds number, and sphericity, the Euclidian distances between samples and W_{ji} are calculated, considering a single jth neuron at each time. The neural network selects the neuron j with the shortest distance in order to group the given sample with the closest center. Then the samples are divided into groups Ω. For all W_{ji}, they are adjusted according to the samples in the groups Ω. For all W_{ji}, the variance of each Gaussian activation function is calculated by using the mean squared distance criterion

$$\sigma_j^2 = \frac{1}{m^{(j)}} \sum_{x^{(k)} \in \Omega^{(j)}} \sum_{i=1}^{n} \left(x_i^{(k)} - W_{ji}^{(1)} \right)^2 \qquad (2)$$

After the first training stage is finished, the steps for adjusting the weights of the neurons in the output layer must be applied. The second training stage are explained as follows. Obtain the original training sample set $\{x^{(k)}\}$ is obtained. The desired output vector $\{d^{(k)}\}$ for each sample is obtained. Initialize $W_{ji}^{(2)}$ with small random values. The learning rate $\{\eta\}$ and required precision $\{\varepsilon\}$ are specified. For all samples $\{x^{(k)}\}$, the values of $g_j^{(1)}$ with respect to the sample $\{x^{(k)}\}$ are obtained; assume $z^{(k)} = [g_1^{(1)} g_2^{(1)} \cdots g_{n_1}^{(1)}]$, $g(.)$ represents an activation function which must be continuous and differentiable in all its domain. Initialize the epoch counter. Repeat the following steps: the mean squared error E_M is back propagated to the previous mean squared error. For all training pairs $\{z(k), d(k)\}$, adjust $W_{ji}^{(2)}$ and θ_j to minimize the error between the outputs produced by the network with respect to the desired outputs. $E_M^{current} \leftarrow E_M$, epoch←epoch+1, until $|E_M^{current} - E_M^{previous}| \leq \varepsilon$. Then the second training process is finished.

2.3. Drag coefficient prediction

First, we predicted drag coefficients applying BPNN and RBFNN, respectively. Pettyjohn et al. [1] experimentally measured the drag coefficients for particles with sphericities of 0.670, 0.806, 0.846, 0.906, and 1.000. Yow et al. [2] collected experimental data from former researchers and made a separation and categorization for the data. Finally, Yow et al. adopted eight sphericities: 0.034, 0.069, 0.140, 0.360, 0.670, 0.820, 0.910 and 1.000. Song et al. [26] investigated the settling behavior and measured drag coefficients of a series of spherical and non-spherical particles, including sphere, cube, and cylinder. Reynolds numbers vary from 0.001 to 100. Sphericity covers 0.471, 0.64, 0.697, 0.756, 0.779, 0.806, 0.873, and 1.000. We employed the data from the work of Pettyjohn et al. and Yow et al. for learning and training, and the data

Table 1
Governing equations and constitutive relations in Eulerian–Eulerian simulation [8].

Conservation of the mass for gas phase and solid phase:

$$\frac{\partial}{\partial t}(\varepsilon_g \rho_g) + \nabla \cdot (\varepsilon_g \rho_g \mathbf{u}_g) = 0 \qquad (5)$$

$$\frac{\partial}{\partial t}(\varepsilon_s \rho_s) + \nabla \cdot (\varepsilon_s \rho_s \mathbf{u}_s) = 0 \qquad (6)$$

$$\varepsilon_g + \varepsilon_s = 1 (7)$$

Conservation of the momentum for gas phase and solid phase:

$$\frac{\partial}{\partial t}(\varepsilon_g \rho_g \mathbf{u}_g) + \nabla \cdot (\varepsilon_g \rho_g \mathbf{u}_g \mathbf{u}_g) = -\varepsilon_g \nabla p + \nabla \cdot \overline{\overline{\tau}}_g + \varepsilon_g \rho_g g - \beta_{gs}(\mathbf{u}_g - \mathbf{u}_s) \qquad (8)$$

$$\frac{\partial}{\partial t}(\varepsilon_s \rho_s \mathbf{u}_s) + \nabla \cdot (\varepsilon_s \rho_s \mathbf{u}_s \mathbf{u}_s) = -\varepsilon_s \nabla p - \nabla p_s + \nabla \cdot \overline{\overline{\tau}}_s + \varepsilon_g \rho_g g - \beta_{gs}(\mathbf{u}_s - \mathbf{u}_g) \qquad (9)$$

Stress tensor for gas phase and solid phase:

$$\overline{\overline{\tau}}_g = \varepsilon_g \mu_g (\nabla \mathbf{u}_g + \nabla \mathbf{u}_g^T) - \frac{2}{3} \varepsilon_g \mu_g (\nabla \cdot \mathbf{u}_g) \overline{\overline{I}} \qquad (10)$$

$$\overline{\overline{\tau}}_s = \varepsilon_s \mu_s (\nabla \mathbf{u}_s + \nabla \mathbf{u}_s^T) + \varepsilon_s (\lambda_s - \frac{2}{3} \mu_s)(\nabla \cdot \mathbf{u}_s) \overline{\overline{I}} \qquad (11)$$

Gas–solid inter-phase momentum exchange coefficient:
Syamlal-O'Brien drag model [42]

$$\beta_{gs} = \frac{3}{4} C_D (\frac{\rho_g \varepsilon_g \varepsilon_s}{d_p v_r^2}) |\mathbf{u}_s - \mathbf{u}_g| \qquad (12)$$

$$v_r = \frac{1}{2}[A - 0.06\,\text{Re}] + \frac{1}{2}[\sqrt{(0.06\,\text{Re})^2 + 0.12\,\text{Re}(2B - A) + A^2}] \qquad (13)$$

$$A = \varepsilon_g^{4.14} (14)$$

$$B = \begin{cases} 0.8\varepsilon_g^{1.28} & \varepsilon_g \leq 0.85 \\ \varepsilon_g^{2.65} & \varepsilon_g > 0.85 \end{cases} \qquad (15)$$

Gidaspow-Blend drag model [43]

$$\beta_{Ergun} = \frac{150\varepsilon_s(1-\varepsilon_g)\mu_g}{\varepsilon_g(\phi d_p)^2} + \frac{1.75\rho_g\varepsilon_s}{\phi d_p}|\mathbf{u}_s - \mathbf{u}_g| \qquad (16)$$

$$\beta_{Wen-Yu} = 0.75 C_D (\frac{\rho_g \varepsilon_g \varepsilon_s}{d_p})|\mathbf{u}_s - \mathbf{u}_g| \varepsilon_g^{-2.65} \qquad (17)$$

$$\varphi_{gs} = \frac{\arctan[150 \times 1.75(0.2 - \varepsilon_s)]}{\pi} + 0.5 \qquad (18)$$

$$\beta_{gs} = (1 - \phi_{gs})\beta_{Ergun} + \phi_{gs}\beta_{Wen-Yu} \qquad (19)$$

Solid phase pressure:

$$p_s = \varepsilon_s \rho_s \theta_s [1 + 2g_0\varepsilon_s(1 + e_{ss})] + p_s^f \qquad (20)$$

Solid shear viscosity:

$$\mu_s = \frac{10\rho_s d_p \sqrt{\pi\theta_s}}{96\varepsilon_s(1 + e_{ss})g_0}[1 + \frac{4}{5}g_0\varepsilon_s(1 + e_{ss})]^2 + \frac{4}{5}\varepsilon_s\rho_s d_p g_0(1 + e_{ss})\sqrt{\frac{\theta_s}{\pi}} + \mu_s^f \qquad (21)$$

Frictional stress model:

$$\mu_s^f = \frac{p_s^f \sin\varphi_f}{2\sqrt{I_{2D}}} \qquad (22)$$

$$I_{2D} = -\frac{1}{2}\overline{\overline{D}} : \overline{\overline{D}} \qquad (23)$$

$$\overline{\overline{D}} = \frac{1}{2}(\nabla\mathbf{u}_s + \nabla\mathbf{u}_s^T) - \frac{1}{3}(\nabla \cdot \mathbf{u}_s)\overline{\overline{I}} \qquad (24)$$

$$p_s^f = \begin{cases} F_r \frac{(\varepsilon_s - \varepsilon_{smin})^m}{(\varepsilon_{smax} - \varepsilon_s)^n} & \varepsilon_s > \varepsilon_{smin} \\ 0 & \varepsilon_s \leq \varepsilon_{smin} \end{cases} \qquad (25)$$

Solid bulk viscosity:

$$F_r = 0.05 N/m^2,\, m = 2,\, n = 5,\, \varepsilon_{smin} = \varepsilon_{smf} \qquad (26)$$

$$\lambda_s = \frac{4}{3}\varepsilon_s\rho_s d_p g_0(1 + e_{ss})\sqrt{\frac{\theta_s}{\pi}} \qquad (27)$$

Radial distribution function:

$$g_0 = [1 - (\frac{\varepsilon_s}{\varepsilon_{smax}})^{1/3}]^{-1} \qquad (28)$$

Conservation of the granular fluctuating energy (algebraic formulation):

$$(-p_s\overline{\overline{I}} + \overline{\overline{\tau}}_s) : \nabla\mathbf{u}_s - \gamma_{\theta s} - 3\beta_{gs}\theta_s = 0 \qquad (29)$$

Collisional dissipation rate of the granular fluctuating energy:

$$\gamma_{\theta s} = \frac{12(1 - e_{ss}^2)g_0}{d_p\sqrt{\pi}}\rho_s\varepsilon_s^2\theta_s^{3/2} \qquad (30)$$

from Song et al. as comparisons. Note that sphericities of 0.670 and 1.000 both appeared in the work of Pettyjohn et al. and Yow et al. We carefully checked the data group and removed repetitive data. By training, the distribution of drag coefficients in the conditions of abovementioned sphericities in Song et al.'s work was predicted. A comparison between prediction and experimental results was conducted. As Fig. 3 illustrated, the predictions using BPNN and RBFNN both approach to the experimental results.

RBFNN is more efficient when predicting the drag coefficient. Under the same condition, the average running time for RBFNN is about 8 s,

compared with 80 s for BPNN. For the prediction of drag coefficient corresponding to diverse sphericities, RBFNN is a reasonable and efficient method and offers a more reasonable theoretical foundation for choosing precise drag coefficient data. Thus, we adopted RBFNN to predict and analyze the drag coefficient under the condition of various sphericities.

To summarize, RBFNN can precisely predict drag coefficient under different sphericities. Furthermore, it can provide a reasonable theoretical basis for calculating the drag coefficient in non-spherical gas–solid system. Sphericities of particles encountered in researches on fluidization usually fall into the range of 0.500 to 1.000. Consequently, in the following step, we predicted drag coefficients with sphericities varying from 0.500 to 1.000. The interval of particle sphericity is 0.02 in the work. Consequently, we obtain adequate data that can be applied to fit curves for drag coefficient, Reynolds number and sphericity. The prediction results are displayed in Fig. 4. We don't put all the curves in the figure, for it is more readable for readers.

2.4. Curve fitting

For a spherical particle, its drag coefficient highly depends on particle Reynolds number. Reynolds regimes are divided into three regions: Stokes' regime (Re < 0.1), intermediate regime (0.1 ≤ Re <1000), and Newton's regime (1000 ≤ Re < 3 × 10^5). In different regimes, fluid flow around spherical particles shows different characteristics. In Stokes' regime, the flow inertial terms are negligible in contrast to viscous terms. The flow keeps attached to sphere with no wake behind. In intermediate regime, a vortex shedding gradually appears and wake behind the sphere increasingly becomes unsteady. In Newton's regime, wakes behind the sphere fully evolves into turbulent flow. There is a laminar boundary layer at the front of the sphere [28]. Similar to the situation of spherical particles, drag coefficient of non-spherical particles is also dependent on particle Reynolds number. In addition, particle shape contributes a lot in determining drag coefficient. A correlation can directly help readers understand the function relationship between the drag coefficient, Reynolds number, and the sphericity. Moreover, it will facilitate the application of the drag model. First we correlated drag coefficient with Reynolds number. Then we found relations between corresponding parameters (A_0, A_1, A_2, A_3, A_4) and sphericity. We keep four digits after the decimal point. When we keep five digits, the R-square is 0.998. It is similar to the situation of keeping four digits after the decimal, with a R-square of 0.998. When we keep three digits, two digits, and one digit, the R-square is 0.949, 0.934, and 0.928, respectively. Fitting results are presented as follows.

$$\lg C_D = A_0 + A_1 \lg Re + A_2 (\lg Re)^2 + A_3 (\lg Re)^3 + A_4 (\lg Re)^4 \quad (3)$$

$$\begin{pmatrix} A_0 \\ A_1 \\ A_2 \\ A_3 \\ A_4 \end{pmatrix} = \begin{pmatrix} -18.5047 & 183.2503 & -613.2826 & 966.0357 & -727.4302 & 211.3367 \\ -12.8162 & 75.0120 & -163.6044 & 150.0228 & -49.4788 & 0 \\ 0.9571 & -7.8929 & 22.3575 & -25.1512 & 9.8015 & 0 \\ 0.4725 & -3.0411 & 5.9850 & -4.2176 & 0.8038 & 0 \\ -0.0480 & 0.4531 & -1.0986 & 0.9621 & -0.2671 & 0 \end{pmatrix} \begin{pmatrix} 1 \\ \phi \\ \phi^2 \\ \phi^3 \\ \phi^4 \\ \phi^5 \end{pmatrix} \quad (4)$$

We employed our equation to calculate drag coefficients for a spherical particle and a non-spherical particle under different Reynolds numbers, respectively. Furthermore, we adopted several widely-accepted correlations [19,21,40,41] to calculate drag coefficients of spherical and non-spherical particles (Figs. 5, 6). Results calculated by our correlation are similar to other typical correlations, indicating its accuracy and applicability for spherical and non-spherical particles.

Table 2
Parameters adopted in the simulation.

Property	Value
h_{bed} (m)	0.5
w_{bed} (m)	0.1
d_{bed} (m)	0.015
h_{pb} (m)	0.1
L_p (mm)	6.0
L_{rod} (mm)	4.5
d_p (mm)	1.5
d_e (mm)	2.6

3. Application of drag model based on two fluid model

To further validate the applicability of our proposed drag model based on the prediction of artificial neural network, it is combined with Two Fluid Model and applied to a series of simulations. The hydrodynamics of several particle systems with different sphericities were numerically investigated. A comparison of simulation and experimental results was conducted.

3.1. Mathematical model

The governing equations and constitutive relations are shown in Table 1.

A universal drag model for spherical particles and nonspherical particles normally takes the voidage, sphericity and Reynolds number into account [44]. The drag coefficient is incorporated into the formula of the inter-phase drag coefficient, which takes solid volume fraction (or voidage) into account. For example, it can be clearly demonstrated in the process of deriving the Gidaspow drag model [45].

The friction coefficients (inter-phase drag coefficients) between the fluid and the solid are obtained from standard correlations with negligible acceleration. With no acceleration, wall friction, or gravity, the gas momentum balance is

$$-\varepsilon_g \frac{\partial P}{\partial x} - \beta_{gs}(v_g - v_s) = 0 \quad (31)$$

This equation is a statement of Darcy's law where the reciprocal of β_{gs} is the permeability divided by the fluid viscosity. The friction coefficient β_A can be obtained by the abovementioned equation. Combined with Ergun equation [46], a new equation of β_A could be got.

$$\beta_{gs} = 150 \frac{(1-\varepsilon_g)^2 \mu_g}{\varepsilon_g (d_p \phi)^2} + 1.75 \frac{\rho_g |v_g - v_s|(1-\varepsilon)}{\phi d_p} \quad (32)$$

The equation is available when ε_g < 0.8.

Wen and Yu [47] extended the works of Richardson and Zaki [48] to derive an expression for pressure drop prediction in a particulate bed. For ε >0.8, if $\partial P/\partial x$ is replaced by Wen and Yu's expression for pressure drop, the friction coefficient in this porosity range becomes

$$\beta_{gs} = \frac{3}{4} C_D \frac{\varepsilon_g |v_g - v_s| \rho_g (1-\varepsilon_g)}{d_p} f(\varepsilon_g) \quad (33)$$

where C_D, the drag coefficient, is related to the Reynolds number by

Table 3
Particle properties and parameters used in the simulation.

Shape	Sphere	Cube	Elongated cuboid	Plate	Elongated plate	Elongated cuboid
d_v (mm)	5	5	5	5	5	5
size (mm)	5	4.2, 4.3, 4.5	3.0, 3.0, 7.1	2.0, 4.9, 6.0	2.0, 4.0, 8.0	2.0, 3.0, 11.0
ϕ (−)	1.00	0.81	0.75	0.71	0.69	0.64
ρ_p (kg/m³)	823.0	639.7	745.6	754.1	756.6	728.1
H_{fb} (mm)	88	98	103	102	108	117
$\bar{\varepsilon}$	0.40	0.37	0.42	0.43	0.46	0.48

Rowe [49]. In this equation, $f(\varepsilon)$ shows the effect due to the presence of other particles in the fluid and acts as a correction to the usual Stokes law for free fall of a single particle. Gidaspow and Ettehadieh [50] have used

$$f(\varepsilon_g) = \varepsilon_g^{-2.65} \tag{34}$$

We combined our drag coefficient correlation with two typical drag models: Syamlal-O'Brien and Gidaspow-blend. For the fixed bed, a combination of our correlation with Syamlal-O'Brien's model was used. In other words, we employed Syamlal-O'Brien's model for the gas velocity less than the minimum fluidization velocity. When the gas velocity surpasses the minimum fluidization velocity, Gidaspow-blend model is adopted. Taghipour et al. [7,51] suggested that Syamlal-O'Brien drag function gives a somewhat better prediction in some cases and it can well predict the hydrodynamics of gas–solid flows. For the fluidized bed, we integrated our correlation with Gidaspow-blend model. Gidaspow drag model uses Ergun equation for $\varepsilon_s \geq 0.2$ and Wen-Yu equation for $\varepsilon_s < 0.2$. It is discontinuous at $\varepsilon_s = 0.2$, which can possibly lead to difficulties in numerical convergence [52]. Gidaspow-blend model combines the results of the Ergun and Wen-Yu drag models to "blend" or smooth the transition when the particle characteristics
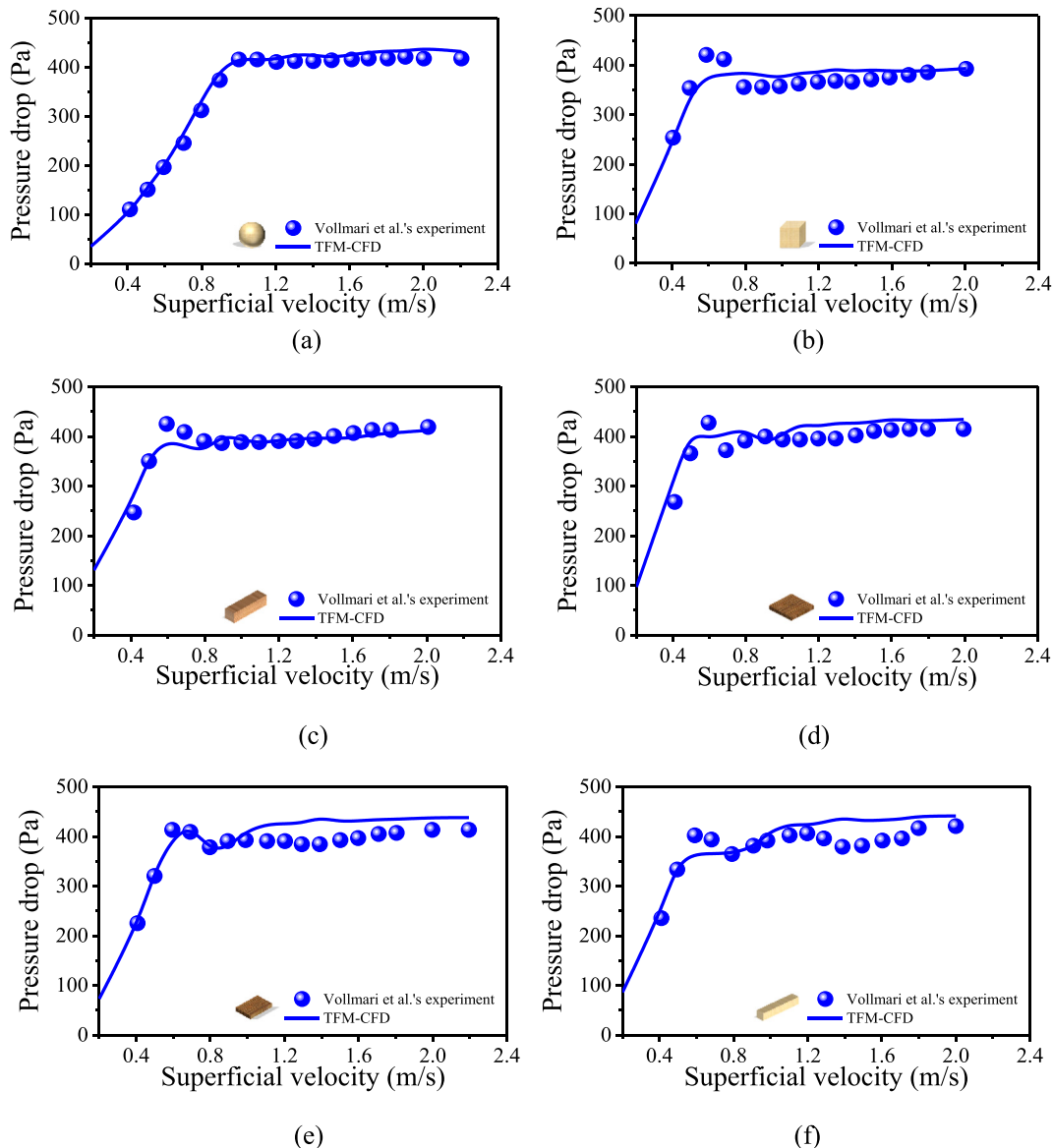

Fig. 7. Pressure drop in experiments[54] and simulations (a) ϕ=1.0 (b) ϕ=0.81 (c) ϕ=0.75 (d) ϕ=0.71 (e) ϕ=0.69 (f) ϕ=0.64.
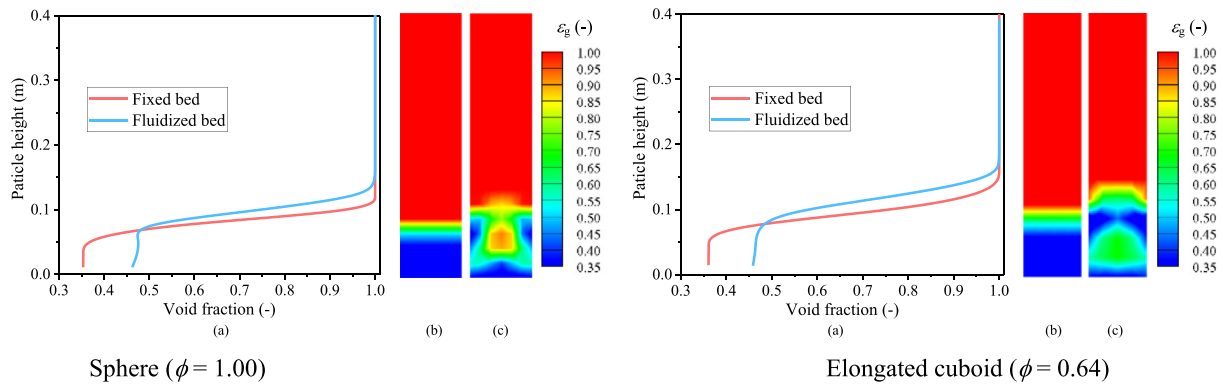
Sphere ($\phi = 1.00$)   Elongated cuboid ($\phi = 0.64$)

Fig. 8. Particle height distribution.

transition from one regime (dilute) to the other (dense). Using the inverse tangent function φ_{gs}, the discontinuity in drag can be overcome.

To validate the effectiveness of the proposed drag model for non-spherical particles, it was adopted to simulate the experimental work Mahajan et al. [53] The case of small-scale spherocylindrical particles in a small-scale fluidized bed was selected. The bed height variation with the superficial gas velocities was studied. A series of TFM simulation were conducted. The cell sizes in the simulations are $20 \times 20 \times 5$ mm^3. The CFD time step is 1.0E-5 s. All the simulations run for 20 s. A velocity inlet and pressure outlet were used as the inflow condition and outlet condition, respectively. A no slip boundary condition was used for the walls. The other parameters used in this part is presented in Table 2.

To further apply our drag model, we used it to simulate Vollmari et al.'s [54] experimental work. A TFM method was applied in the simulation. We studied the pressure drop of particles with the same equivalent surface sphere diameter (5 mm) and different shapes (sphere, cube, elongated cuboid, plate, elongated plate, and elongated cuboid). Comparison results were presented in Fig. 6. Cell sizes in the TFM-CFD simulations are $22 \times 22 \times 25.5$ mm^3. The CFD time step is 1.0E-5 s. All the simulations run for 20 s. A velocity inlet and pressure outlet were used as the inflow condition and outlet condition, respectively. A no slip boundary condition was used for the walls. Particle properties are presented in Table 3.

3.2. Results and discussion

Fig. 6 show the variation of bed height under different superficial gas velocities. The simulation results are in the range of experimental errors. In summary, the simulation results agree well with the experimental data. It denotes that the proposed drag model can well describe the interaction between the gas phase and the solid phase. The bed height almost remains constant at the onset of channeling. With the increase of the superficial gas velocity, the bed height gradually increases. At the high superficial gas velocities, there is a strong fluctuation.

Fig. 7a shows the results of simulation and experiment of spherical particles. Numerical examination agrees well with experimental examination. Fig. 7b displays outcome for cubes with the dimensions of 4 mm × 4 mm × 4 mm. It is distinct that experiment and simulation are in a good agreement. When the superficial gas velocity exceeds the minimum fluidization velocity (0.8 m/s), experimental results instantly decline. Interlocking between the particles is the major factor of this decline [54,55]. The interlocking between cubes is of a much greater magnitude than that of the spheres. Fig. 7c provides results of 3 mm × 3 mm × 7 mm cuboids. The average deviation for the fixed bed is 25.6 Pa, while it is 120 Pa in the Vollmari et al. [54]' s work. When the bed is fluidized ($u_{sp} > 0.8$ m/s), the average deviation of pressure drop is 15.6 Pa, compared with 18 Pa in the experiments. In the experiments, stacks of particles rest in the corners and at the walls of the

vessel. This results in a partial fluidization and furthermore leads to the difference in the pressure drop for the fluidized regime. Fig. 7d shows the outcome of 2 mm × 5 mm × 6 mm plates. The average deviation for the pressure drop over the entire velocity range is 25.7 Pa, compared with 35 Pa of the simulation results of Vollmari et al.[54]. Fig. 7e gives the results of 2 mm × 4 mm × 8 mm elongated plates. There is a good agreement between experiment and simulation for the entire velocity range with average deviations of 24.9 Pa, while it is 40 Pa in Vollmari et al.'s work. Partial fluidization in the experiment leads to an average deviation between the experiment and TFM-CFD of 31.2 Pa for the fluidized bed regime ($u_{sp} > 0.8$ m/s). Fig. 7f displays outcome for 2 mm × 3 mm × 11 mm elongated cuboids. According to Emden et al. [55], elongated particles tend to form channeling instead of undergoing smooth fluidization. Then both the entire bed and particles within the channels are in motion. The average deviation for the pressure drop of the fixed bed ($u_{sp} < 0.6$ m/s) is 21.9 Pa. Partial fluidization leads to an overestimation of the pressure drop for the fluidized range ($u_{sp} > 0.8$ m/s). The average deviation for this region is 29.4 Pa.

Fig. 8 presents particle height distribution for two kinds of previously mentioned particles. For each kind of particle, Fig. a shows particle height varying with void fraction in fixed bed and fluidized bed, respectively. Figs. b and c give instantaneous void fraction distribution for fixed bed and fluidized bed. Void fraction increases with increasing particle height. In the beginning, the void fraction for the fixed bed is less than that for the fluidized bed at the same bed height. The fluidized bed reaches the largest void fraction faster than the fixed bed. For fixed beds, particles are not fully fluidized. Hence, the state of bed is almost the same. According to the contour plot (Figs. b and c), it is found that there is a difference between the fluidization state of spherical and non-spherical particles. Note that the shape of bubbles is different. The boundary shape of a bubble in the fluidized bed with spherical particles is more regular. In contrast, it is not that regular in the fluidized bed with non-spherical particles.

4. Conclusions

In this work, ANN is used to predict and analyze drag coefficients for non-spherical particles. Comparisons between simulations and experiments were conducted.

Results demonstrate that ANN is an efficient tool in predicting drag coefficients of non-spherical gas–solid system. Using RBFNN is more efficient and saves more computing time. In conclusion, applying ANN can well predict drag coefficient under different sphericities. Note that the influence of sphericity on drag coefficient is not negligible. The drag coefficient correlation proposed by us can accurately predict drag coefficients of spherical particles and non-spherical particles. It efficiently facilitates investigating hydrodynamic characteristics of gas–solid flow.

We applied a CFD model based on the Eulerian-Eulerian approach. The proposed drag model is combined with two typical drag models.

For the fixed bed, the proposed drag model employed Symlal-O'Brien correlation. Our model is available for Reynolds number ranging from 0.01 to 10,000. For the fluidized bed, Gidaspow-blend correlation was used. To validate our proposed drag model, we applied it to simulate Mahajan et al.'s experiments. The predicted results of bed height agree well with the experimental results. It denotes that our drag model can accurately describe the drag force of particles in fixed beds and fluidized beds. The shape of bubbles is different. Moreover, we applied the proposed drag model to simulate the experiment of Vollmari et al. The simulation results are in well agreement with the experimental data. In addition, the fluidization state of fluidized bed with spherical and non-spherical particles is different. Furthermore, our work can be a reference for predicting drag coefficients and constructing gas–solid drag models in non-spherical particulate systems.

Nomenclature

C_D	drag coefficient (dimensionless)
$\overline{\overline{D}}$	rate of strain tensor of the solid phase (s^{-1})
d_e	volume equivalent spherical diameter (m)
d_{bed}	bed depth (m)
d_p	particle diameter (m)
$d^{(k)}$	the desired ouput vector
$E_M^{current}$	the mean squared error in the current epoch
$E_M^{previous}$	the mean squared error in the previous epoch
e_{ss}	particle–particle restitution coefficient (dimensionless)
F_r	constant in equation for p_s^f (N/m^2)
g	gravitational constant (m/s^2)
g_0	radial distribution function (dimensionless)
H_{fb}	fixed bed height (m)
h_{bed}	bed height (m)
h_{pb}	packed bed height (m)
$\overline{\overline{I}}$	unit tensor (dimensionless)
I_{2D}	second invariant of the deviator of the strain rate tensor of solid phase (s^{-2})
L_p	particle length (m)
p_s	solid phase pressure (Pa)
L_{rod}	rod length (m)
p_s^f	solid frictional pressure (Pa)
Re	Reynolds number (dimensionless)
u_g	gas velocity (m/s)
u_s	solid velocity (m/s)
u_{sp}	superficial velocity (m/s)
v_r	relative velocity correlation (dimensionless)
$W_{ji}^{(1)}$	the value of the synaptic weight connecting jth neuron to the ith neuron in the first training stage
W_{bed}	bed width (m)
$W_{ji}^{(2)}$	the value of the synaptic weight connecting jth neuron to the ith neuron in the second training stage
$x^{(k)}$	the original training sample set
$Y_j(k)$	the value produced by the jth output neuron of the network for the kth training sample

Greek symbol

β_{gs}	inter-phase drag coefficient (kg/m^{3}s)
β_{Ergun}	drag coefficient calculated by Ergun correlation (kg/m^{3}s)
B_{Wen-Yu}	drag coefficient calculated by Wen-Yu correlation (kg/m^{3}s)
$\gamma_{\theta s}$	collisional dissipation rate of the granular fluctuating energy (kg/ms^3)
ε	learning precision
ε_g	gas void fraction (dimensionless)
ε_s	solid void fraction (dimensionless)
ε_{smax}	solid volume fraction at the maximum packing state (dimensionless)
ε_{smin}	solid volume fraction beyond which frictional force occurs (dimensionless)
η	learning rate
θ_j	threshold from the output layer neurons
θ_s	granular temperature (m^2/s^2)
λ_s	solid bulk viscosity (Pa s)
μ_g	gas viscosity (Pa s)
μ_s	solid shear viscosity (Pa s)
ρ_g	gas density (kg/m^3)
ρ_s	solid density (kg/m^3)
$\overline{\overline{\tau}}_g$	stress tensor for the gas phase (Pa)
$\overline{\overline{\tau}}_s$	stress tensor for the solid phase (Pa)
ϕ	sphericity (dimensionless)
φ_f	internal friction angle of particles (degree)
φ_{gs}	blending function (dimensionless)

Acknowledgement

References

[1] E.S. Pettyjohn, Effect of particle shape on free settling rates of isometric particles, Chem. Eng. Prog. 44 (1948) 157–172.

[2] H.N. Yow, M.J. Pitt, A.D. Salman, Drag correlations for particles of regular shape, Adv. Powder Technol. 16 (2005) 363–372.

[3] N.G. Deen, J.A.M. Kuipers, Direct numerical simulation of fluid flow accompanied by coupled mass and heat transfer in dense fluid–particle systems, Chem. Eng. Sci. 116 (2014) 645–656.

[4] N.G. Deen, E.A.J.F. Peters, J.T. Padding, J.A.M. Kuipers, Review of direct numerical simulation of fluid–particle mass, momentum and heat transfer in dense gas–solid flows, Chem. Eng. Sci. 116 (2014) 710–724.

[5] J.E. Hilton, L.R. Mason, P.W. Cleary, Dynamics of gas–solid fluidised beds with non-spherical particle geometry, Chem. Eng. Sci. 65 (2010) 1584–1596.

[6] F. Dioguardi, D. Mele, A new shape dependent drag correlation formula for non-spherical rough particles, experiments and results, Powder Technol. 277 (2015) 222–230.

[7] F. Taghipour, N. Ellis, C. Wong, Experimental and computational study of gas–solid fluidized bed hydrodynamics, Chem. Eng. Sci. 60 (2005) 6857–6867.

[8] L. Hua, H. Zhao, J. Li, J. Wang, Q. Zhu, Eulerian–Eulerian simulation of irregular particles in dense gas–solid fluidized beds, Powder Technol. 284 (2015) 299–311.

[9] D. Escudero, T.J. Heindel, Bed height and material density effects on fluidized bed hydrodynamics, Chem. Eng. Sci. 66 (2011) 3648–3655.

[10] V. Verma, N.G. Deen, J.T. Padding, J.A.M. Kuipers, Two-fluid modeling of three-dimensional cylindrical gas–solid fluidized beds using the kinetic theory of granular flow, Chem. Eng. Sci. 102 (2013) 227–245.

[11] Y. Chen, J.R. Third, C.R. Müller, A drag force correlation for approximately cubic particles constructed from identical spheres, Chem. Eng. Sci. 123 (2015) 146–154.

[12] M. Nikku, P. Jalali, J. Ritvanen, T. Hyppänen, Characterization method of average gas–solid drag for regular and irregular particle groups, Powder Technol. 253 (2014) 284–294.

[13] M. Mandø, L. Rosendahl, On the motion of non-spherical particles at high Reynolds number, Powder Technol. 202 (2010) 1–13.

[14] G. Lu, J.R. Third, C.R. Müller, Discrete element models for non-spherical particle systems: from theoretical developments to applications, Chem. Eng. Sci. 127 (2015) 425–465.

[15] J.Q. Gan, Z.Y. Zhou, A.B. Yu, Micromechanical analysis of flow behaviour of fine ellipsoids in gas fluidization, Chem. Eng. Sci. 163 (2017) 11–26.

[16] J.E. Hilton, P.W. Cleary, The influence of particle shape on flow modes in pneumatic conveying, Chem. Eng. Sci. 66 (2011) 231–240.

[17] M. Zastawny, G. Mallouppas, F. Zhao, B. Wachem, Derivation of drag and lift force and torque coefficients for non-spherical particles in flows, Int. J. Multiphas. Flow. 39 (2012) (2012) 227–239.

[18] A. Hölzer, M. Sommerfeld, Lattice Boltzmann simulations to determine drag, lift and torque acting on non-spherical particles, Comput. Fluids 38 (2009) 572–589.

[19] A. Haider, O. Levenspiel, Drag coefficient and terminal velocity of spherical and non-spherical particles, Powder Technol. 58 (1989) 63–70.

[20] P.K. Swamee, C.S.P. Ojha, Drag coefficient and fall velocity of nonspherical particles, J. Hydraul. Eng. 117 (1991) 660–667.

[21] G.H. Ganser, A rational approach to drag prediction of spherical and nonspherical particles, Powder Technol. 77 (1993) 143–152.

[22] R.P. Chhabra, L. Agarwal, N.K. Sinha, Drag on non-spherical particles: an evaluation of available methods, Powder Technol. 101 (1999) 288–295.

[23] S.F. Chien, Settling velocity of irregularly shaped particles, Spe. Drill Compl. 9 (1994) 281–289.

[24] M. Hartman, O. Trnka, K. Svoboda, V. Veselý, Influence of particle shape on the drag coefficient for isometric particles, Collect. Czechoslov. Chem. Commun. 59 (1994) 2583–2594.

[25] S. Tran-Cong, M. Gay, E.E. Michaelides, Drag coefficients of irregularly shaped particles, Powder Technol. 139 (2004) 21–32.

[26] X. Song, Z. Xu, G. Li, Z. Pang, Z. Zhu, A new model for predicting drag coefficient and settling velocity of spherical and non-spherical particle in Newtonian fluid, Powder Technol. 321 (2017) 242–250.

[27] G.H. Bagheri, C. Bonadonna, I. Manzella, P. Pontelandolfo, P. Haas, Dedicated vertical wind tunnel for the study of sedimentation of non-spherical particles, Rev. Sci. Instrum. 84 (2013), 054501.

[28] G.H. Bagheri, C. Bonadonna, On the drag of freely falling non-spherical particles, Powder Technol. 301 (2016) 526–544.

[29] S. Shanmuganathan, S. Samarasinghe, Artificial Neural Network Modelling, Springer, 2016.

[30] W.S. McCulloch, W. Pitts, A logical calculus of the ideas immanent in nervous activity, Bull. Math. Biophys. 5 (1943) 115–133.

[31] D.O. Hebb, The Organization of Behavior: A Neuropsychological Approach, John Wiley & Sons, 1949.

[32] I.N. Silva, D. Hernane Spatti, R. Andrade Flauzino, L.H.B. Liboni, S.F. dos Reis Alves, Artificial Neural Networks, Springer International Publishing, Cham, 2017.

[33] S.B. Maiti, S. Let, N. Bar, S.K. Das, Non-spherical solid-non-Newtonian liquid fluidization and ANN modelling: minimum fluidization velocity, Chem. Eng. Sci. 176 (2018) 233–241.

[34] A.A.K. Farizhandi, H. Zhao, R. Lau, Modeling the change in particle size distribution in a gas–solid fluidized bed due to particle attrition using a hybrid artificial neural network-genetic algorithm approach, Chem. Eng. Sci. 155 (2016) 210–220.

[35] L. Yu, S. Wang, K.K. Lai, Foreign-Exchange-Rate Forecasting with Artificial Neural Networks, Springer Science & Business Media, 2010.

[36] D.E. Rumelhart, G.E. Hinton, R.J. Williams, Learning internal representations by error propagation, Read. Cognit. Sci. 1 (1988) 399–421.

[37] D. Graupe, Principles of Artificial Neural Networks, World Scientific, 2007.

[38] D.S. Broomhead, D. Lowe, Radial basis functions, multi-variable functional interpolation and adaptive networks, Advances in Neural Information Processing Systems, Rsre-Memo-4148 1988, pp. 728–734.

[39] J. Liu, Radial Basis Function (RBF) Neural Network Control for Mechanical Systems: Design, Analysis and Matlab Simulation, Springer Science & Business Media, 2013.

[40] L. Schiller, A. Naumann, Fundamental calculations in gravitational processing, Zeitschrift Des Vereines Deutscher Ingenieure 77 (1933) 318–320.

[41] A. Hölzer, M. Sommerfeld, Lattice Boltzmann simulations to determine drag, lift and torque acting on non-spherical particles, Comput. Fluids 38 (2009) 572–589.

[42] M. Syamlal, T.J. O'Brien, Computer simulation of bubbles in a fluidized bed, AIChE Symp. Ser. 85 (1989) 22–31.

[43] D. Lathouwers, J. Bellan, Modeling and Simulation of Bubbling Fluidized Beds Containing Particle Mixtures, Proc. Combust. Inst. 28 (2000) 2291–2304.

[44] Y. Tang, E. Peters, J.A.M. Kuipers, S.H.L. Kriebitzsch, M.A. van der Hoef, A new drag correlation from fully resolved simulations of flow past monodisperse static arrays of spheres, AICHE J. 61 (2015) 688–698.

[45] D. Gidaspow, Multiphase Flow and Fluidization: Continuum and Kinetic Theory Descriptions, Academic Press, 1994.

[46] S. Ergun, Fluid flow through packed columns, Chem. Eng. Prog. 48 (1952) 89–94.

[47] C.Y. Wen, Y.H. Yu, Mechanics of fluidization, Chem. Eng. Prog. Symp. Ser. 62 (1966) 100–111.

[48] J.F. Richardson, W.N. Zaki, The sedimentation of a suspension of uniform spheres under conditions of viscous flow, Chem. Eng. Sci. 3 (1954) 65–73.

[49] P.N. Rowe, Drag forces in a hydraulic model of a fluidised bed-part II, Trans. Instrum. Chem. Eng. 39 (1961) 175–180.

[50] D. Gidaspow, B. Ettehadieh, Fluidization in two-dimensional beds with a jet. Part II: hydrodynamic modeling, Ind. Eng. Chem. Fundam. 22 (1983) 193–201.

[51] S. Zimmermann, F. Taghipour, CFD Modeling of the hydrodynamics and reaction kinetics of FCC fluidized-bed reactors, Ind. Eng. Chem. Res. 44 (2005) 9818–9827.

[52] H. Lu, D. Gidaspow, Hydrodynamics of binary fluidization in a riser: CFD simulation using two granular temperatures, Chem. Eng. Sci. 58 (2003) 3777–3792.

[53] V.V. Mahajan, J.T. Padding, T.M. Nijssen, K.A. Buist, J.A.M. Kuipers, Nonspherical particles in a pseudo-2D fluidized bed: experimental study, AICHE J. 64 (2018) 1573–1590.

[54] K. Vollmari, R. Jasevičius, H. Kruggel-Emden, Experimental and numerical study of fluidization and pressure drop of spherical and non-spherical particles in a model scale fluidized bed, Powder Technol. 291 (2016) 506–521.

[55] H. Kruggel-Emden, K. Vollmari, Flow-regime transitions in fluidized beds of non-spherical particles, Particuology. 29 (2016) 1–15.